Journal of Bioscience and Bioengineering
VOL. 109 No. 6, 588 – 597, 2010

ELSEVIER

www.elsevier.com/locate/jbiosc

Computational fluid dynamics modeling of gas dispersion in multi impeller bioreactor

Syed Ubaid Ahmed,[1] Panneerselvam Ranganathan,[2] Ashok Pandey,[1] and Savithri Sivaraman[2,*]

Biotechnology Division, National Institute for Interdisciplinary Science and Technology (CSIR), Trivandrum-695 019, India[1] *and Computational Modeling and Simulation Section, National Institute for Interdisciplinary Science and Technology (CSIR), Trivandrum- 695 019, India*[2]

Received 9 September 2009; accepted 18 November 2009
Available online 19 January 2010

In the present study, experiments have been carried out to identify various flow regimes in a dual Rushton turbines stirred bioreactor for different gas flow rates and impeller speeds. The hydrodynamic parameters like fractional gas hold-up, power consumption and mixing time have been measured. A two fluid model along with MUSIG model to handle polydispersed gas flow has been implemented to predict the various flow regimes and hydrodynamic parameters in the dual turbines stirred bioreactor. The computational model has been mapped on commercial solver ANSYS CFX. The flow regimes predicted by numerical simulations are validated with the experimental results. The present model has successfully captured the flow regimes as observed during experiments. The measured gross flow characteristics like fractional gas hold-up, and mixing time have been compared with numerical simulations. Also the effect of gas flow rate and impeller speed on gas hold-up and power consumption have been investigated.

[**Key words:** Computational fluid dynamics (CFD); Multiphase flow; Bubble size; Gas dispersion; Mixing; Stirred tank]

Gas–liquid stirred reactors with multiple impellers are used in several industrial applications like fermentations, waste water treatment, hydrogenation, dissolution, etc. Multiple impellers are often used in industrial applications to increase the efficiency of an agitated tank because the ratio between liquid height and tank diameter is usually larger than unity. Also stirred reactors with multiple impellers provide better gas utilization, higher interfacial area and narrower residence time distribution in the flow system compared to a single impeller stirred reactor. Also the multiple impeller systems are preferred in bioreactors, as they offer lower average shear as compared to single impeller system and allow more degrees of freedom for controlling the gas dispersion as well as the bulk flow of liquid phase at equivalent power dissipation rate and are now becoming important due to their efficient gas-distribution and better oxygen utilization characteristics, higher gas phase residence time, increased gas hold-up and superior liquid flow (plug flow) characteristics (1).

The complete dispersion of gas is the most desirable and important requirement for any mechanically agitated contactor. The gas dispersion in a stirred tank is extremely complex with the possibility of several dispersion regimes (flooding, loading, complete dispersion, recirculation of gas–liquid mixture) depending upon the type of impeller, speed of agitation, superficial gas velocity, sparger size, type, and location. These different flow regimes show different fluid dynamic conditions in the reactor and therefore, can have different rates of transport as well as mixing processes. In literature, various authors (2–6) have investigated flow patterns for gas–liquid contactor agitated by different multiple impeller combinations and some of authors (5, 7–10) have studied the effect of the impeller speed and the gas velocity on the mixing time. Recently, Shewale and Pandit (11) have experimentally studied the mixing process occurring in an aerated stirred reactor equipped with three down-pumping six-blade pitched turbine operating in different gas flow regimes. They have found significant influence of the prevailing gas flow regimes on the time scale of the mixing process occurring in the reactor.

During the last two decades, computational fluid dynamics (CFD) techniques have been used to calculate the fluid flow in agitated tanks. Advances in computer technology and CFD software have encouraged researchers to develop simulations of gas dispersion and solid suspension performance. In recent years, several studies have been reported on computational modeling of gas–liquid flows in stirred reactors (12–15). Wang and Mao (16) used an improved inner-outer iterative procedure to treat the region agitated by a Rushton impeller in a gas–liquid reactor. Lane et al. (17) used several alternative treatments of the multiphase equations and also considered variations in bubble size resulting from coalescence and breakup in an aerated vessel stirred by a Rushton turbine. Alves et al. (18) experimentally investigated gas dispersion in a stirred tank with a double turbine agitator. Alves et al. (19) used a compartment model that takes into account the combined effect of bubble coalescence and breakage to simulate gas dispersion in a double turbine stirred tank. Reasonable agreement between their experiment and simulation is achieved with optimization of two parameters, one affecting mainly the slip velocity, the other related mainly to the bubble coalescence/

* Corresponding author. Tel.: +91 471 2515264; fax: +91 471 2491712.
E-mail address: sivakumarsavi@gmail.com (S. Sivaraman).

1389-1723/$ - see front matter © 2009, The Society for Biotechnology, Japan. All rights reserved.
doi:10.1016/j.jbiosc.2009.11.014

Nomenclature

a	specific area, m^{-1}
B	birth source, kg/m^3 s
B_{ij}	specific breakup rate, 1/s
C_B	constant, dimensionless
$C_{D,lg}$	drag coefficient between liquid and gas phase
C_D	drag coefficient in turbulent liquid
C_{ij}	specific coalescence rate, m^3/s
C_{D0}	drag coefficient in stagnant liquid
C_{TD}	turbulent dispersion coefficient
$C\mu,\sigma_k, \sigma_\varepsilon, C_{\varepsilon 1}, C_{\varepsilon 2}$	coefficient in turbulent parameters
D	impeller diameter, m
$C\mu_p$	coefficient in particle induced turbulence model
D	death source, kg/m^3 s
d_b	bubble mean diameter, m
$E(\alpha_g)$	correction term, dimensionless
Eo	Eotvos number, dimensionless
f_i	ith group fraction
f_{BV}	breakup fraction, dimensionless
F_C	calibration coefficient
$F_{D,lg}$	interphase drag force between liquid and gas, N
Fl	flow number, dimensionless
Fr	Froude number, dimensionless
$\underline{F}_{TD}$	turbulent dispersion Force, N
g	gravitational acceleration, m/s^2
h_0	*initial* film thickness, m
h_f	critical film thickness, m
k	the turbulence kinetic energy, m^2/s^2
m	group mass
n	number density, $1/m^3$
N	total number of bubble class
N_{Pg}	areated power number
N_{P0}	power number
P	power, w
P	liquid-phase pressure, kg/m^1 s^2
P_α	turbulence production due to viscous and buoyancy forces
r_{ij}	equivalent radius, m
Re_b	bubble Reynolds number
R	radial position, m
S	source term, kg/m^3 s
S_{ij}	cross-sectional area of the colliding, m^2
t	time, s
t_{ij}	time required for coalescence, s
T	Total torque,
$u\rightarrow_g$	local gas phase velocity vector, m/s
$u\rightarrow_l$	local liquid phase velocity vector, m/s
u_{ti}	turbulent velocity, m/s
v	volume of bubbles, m^3
X_{jki}	mass fraction, dimensionless
z	axial position, m

Greek letters

ε_l, ε_g, ε_s	liquid, gas and solid volume fraction respectively
ε	liquid phase turbulence eddy dissipation, m^2/s^3
η_{ij}	collision efficiency, dimensionless
ρ_g	gas density, kg/m^3
ρ_l	liquid density, kg/m^3
$\Delta\rho$	density difference between liquid and gas, kg/m^3
$\mu_{eff,g}$	gas phase effective viscosity, kg /m s^2
$\mu_{eff,l}$	liquid phase effective viscosity, kg /m s^2
μ_g	gas viscosity, kg /m s^2
μ_l	liquid viscosity, kg /m s^2
μ_{tg}	gas induced turbulence viscosity, kg /m s^2
$\mu_{T,l}$	liquid induced turbulence viscosity, kg /m s^2
$\mu_{T,g}$	gas induced turbulence viscosity, kg /m s^2
σ	surface tension force, N/m
σ_k	constant, dimensionless
$\sigma\varepsilon$	constant, dimensionless
β	constant, dimensionless
τ_{ij}	actual time during the collision, s
υ	kinematic viscosity, m^2/s
ξ	dimensionless size of eddies in the inertial subrange of isotropic turbulence, dimensionless

Subscripts and superscripts

k	phase
l	liquid phase
g	gas phase
i	ith bubble group
j	jth bubble group
k	kth bubble group
eff	effective
FF	flooding regime in both impellers
DL	dispersed in upper impeller and loading regime in lower impeller
DD	dispersed regime in both impeller
max	maximum
min	minimum
rpm	revolution per minute
Rps	revolution per second
RT	Rushton turbine
vvm	volume of gas per volume of slurry per minute

breakage balance. Kerdouss et al. (20) modeled the gas dispersion in a double turbine baffled stirred tank using a commercial computational fluid dynamics (CFD) code FLUENT 6.1 (Fluent Inc., USA) using multiple reference model. A bubble number density equation is implemented in order to account for the combined effect of bubble break-up and coalescence in the tank. The numerical results were compared with experimental work (18). Khopkar et al. (21) used a two fluid model, along with the standard k–ε turbulence model, to simulate dispersion in a gas–liquid flow. They captured qualitatively the overall flow field generated by three down pumping pitched-blade turbines, including the liquid circulation loops and the quality of gas dispersion in the reactor for all three flow regions. Most of previous studies used single bubble size to study the gas dispersion in stirred tank rather than considering the effects of bubble breakup and coalescence and only few studies included bubble size distribution in their work. Similarly, none of the reported studies was able to quantitatively simulate the gas–liquid flows in different flow regimes prevailing in the reactor. Considering the limitations of the published studies, it becomes essential to develop computational model to predict the flow characteristics of the gas–liquid flows generated by multiple impellers in bioreactor.

Thus in this work, we aim at gaining insight in the flow regimes and prediction of hydrodynamics parameters, gas holdup, local bubble-size distributions and mixing time in a vessel agitated by dual Ruston turbine impellers. Eulerian multiphase and population balance equation-multiple size group (MUSIG) models have been implemented. Breakup and coalescence of bubbles are modeled fundamentally using isotropic turbulence theory. The flow regimes predicted by numerical simulations are validated with our own experimental results. The gross flow characteristics like fractional gas hold-up, and mixing time have been measured and compared with numerical simulations.

MATERIALS AND METHODS

The schematic diagram of experimental setup is shown in Fig. 1. Experiments were conducted in a baffled cylindrical acrylic vessel of internal diameter 160 mm and height 250 mm with dual impellers mounted on the shaft. Baffles having a width of 12 mm were placed perpendicular to the vessel. The first impeller was located at a distance of 80 mm from the bottom of the vessel and the spacing between the first and second impeller is 110 mm. Air was sparged to the tank through a ring sparger of diameter 52 mm with 16 symmetrically drilled holes of 1 mm diameter and was located at a distance of 5 mm from the bottom of the vessel. The type of impeller used was six-bladed Rushton turbine diameter of 64 mm with blade height of 13 mm and width of 19 mm. Experiments were conducted with tap water. The vessel was filled with water up to a height of 240 mm. The flow rate of sparged air were 0.3, 0.5, 1.0 vvm. The impeller rotation speed was from 200 to 600 rpm. The gas hold-up was found by visual observation method. In this method, the dispersed height is measured in the presence and absence of aeration and the following equation is used for gas hold-up:

$$\varepsilon_g = \frac{(H_g - H_i)}{H_g} \tag{1}$$

where H_g is the final dispersed height and H_i is the initial liquid height.

This method was also implemented and verified by Shewale and Pandit (11) in a multiple agitated vessel. The power consumed by the impeller was found by using the clamp on meter. The equation used for calculation of impeller power consumption is given as

$$P = VI \cos \varphi \tag{2}$$

where V is the voltage, I is the current and cos φ is the power factor and is taken as 0.95.

The flow regimes for gas–liquid stirred reactor agitated with dual impellers were identified by visual observation and by taking the images of vessel using digital camera. For calculation of mixing time, the pH measurement method was employed with HCl as tracer fluid. Using acrylic tube, a known volume of tracer was dumped on the bulk liquid. The change in the pH of the bulk liquid along the height of the vessel was recorded with the help of two pH probes. These pH probes were located just below each impeller plane, and these probes give an accurate estimation of the mixing time in each impeller zone.

Basic governing equations In this work, a 3D transient CFD model is developed to simulate the local hydrodynamics of the gas–liquid stirred reactor agitated by a dual impeller system. An Eulerian approach is adapted to describe the flow behavior of each phase. Liquid phase is considered as a continuous phase while the gas phase is considered as a polydispersed phase, where there is a large variation in size. One of the attributes of polydispersed multiphase flow is that the different sizes of the dispersed phases interact with each other through the mechanism of breakup and coalescence. The polydispersed gas phase is characterized by a volume fraction and a diameter coming from a preliminary bubble size distribution. For the present simulation, 10 bubble classes with diameters ranging from 1 to 11 mm are considered, based on the equal diameter discretization criteria. That means, the diameter of group i is calculated from Eq. (3) as

$$d_i = d_{min} + \Delta d\left(i - \frac{1}{2}\right)$$
$$\Delta d = \frac{d_{max} - d_{min}}{N} \tag{3}$$

where d_{min}, d_{max} correspond to the minimum and maximum diameter of the polydispersed phase and the group mass is calculated from the Eq. (4)

$$m = \frac{\pi}{6}\rho_d d^3 \tag{4}$$

Hence a system of 11 equations (1 momentum and 10 continuity equations) is solved for the gas phase, combined with a system of two equations for the liquid phase. Euler–Euler Reynolds-averaged continuity and momentum transport equations are written for each phase as

Continuity equations The continuity equation for the liquid phase is given by

$$\frac{\partial}{\partial t}(\in_l \rho_1) + \nabla \cdot \left(\rho_1 \in_l \vec{u_1}\right) = 0 \tag{5}$$

where ρ_l is the density and $\in_l$ is the volume fraction of the continuous liquid phase. The continuity equation for the poly dispersed gas phase is derived from the population balance equation which represents the continuity of particles of size υ. Let $n(\upsilon,t)$ represent the number density of particles of size υ at time t. Then the population balance equation is

$$\frac{\partial}{\partial t}(n(\upsilon,t)) + \nabla \cdot \left(n(v,t)\vec{u}_g\right) = B_B - D_B + B_c - D_c \tag{6}$$

The above equation is discretized into size groups. Let N_i represent the number density of group i.

$$N_i(t) = \int_{\upsilon_{i-1/2}}^{\upsilon_{i+1/2}} n(\upsilon,t)\mathrm{d}t \tag{7}$$

Let the mass and volume fraction of group i be m_i, ε_i respectively and we have the following relation:

$$\rho_i \varepsilon_i = m_i N_i \tag{8}$$

Integrating the equation over the bin size dimension and multiplying by m_i we get the following equation:

$$\frac{\partial}{\partial t}(\rho_i \varepsilon_i) + \nabla.\left(\rho_i \varepsilon_i \vec{u_g}\right) = S_i \tag{9}$$

By defining the size fraction as

$$f_i = \frac{\varepsilon_i}{\varepsilon_g} \tag{10}$$

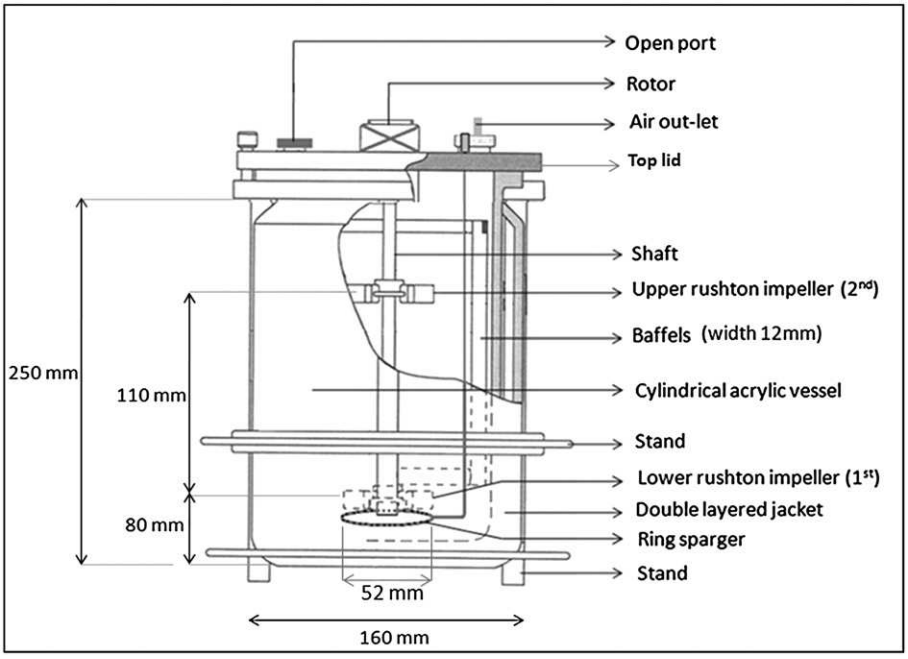

FIG. 1. The schematic diagram of experimental setup.

Eq. (9) simplifies to

$$\frac{\partial}{\partial t}(\rho_i \varepsilon_g f_i) + \nabla.\left(\rho_i \varepsilon_i f_i \vec{u_g}\right) = S_i \tag{11}$$

A further simplification is made to this equation by assuming that all size groups share the same density and velocity yielding the continuity equation

$$\frac{\partial}{\partial t}(\varepsilon_g \cdot \rho_g f_i) + \nabla.\left(\rho_g \cdot \varepsilon_g f_i \cdot \vec{u_g}\right) = S_i \tag{12}$$

where ρ_g is the density and $\in_g$ is the volume fraction of the dispersed gas phase.

The source term represents birth and death due to breakup and coalescence and is given by

$$S_i = B_{B_i} - D_{B_i} + B_{C_i} - D_{C_i} \tag{13}$$

and the following constraint must be satisfied by the source term S_i

$$\sum_i S_i = 0 \tag{14}$$

The volume fraction of the two phases satisfies the following condition:

$$\in_1 + \in_g = 1 \tag{15}$$

Momentum equations Liquid phase (continuous phase)

$$\frac{\partial}{\partial t}\left(\rho_1 \cdot \in_1 \cdot \vec{u_1}\right) + \nabla.\left(\rho_1 \cdot \in_1 \cdot \vec{u_1}\vec{u_1}\right) = \in_1.\nabla P + \nabla.\left(\in_1 \mu_{\text{eff},1}\left(\nabla \vec{u_1} + \left(\nabla \vec{u_1}\right)^T\right)\right) + \rho_1 \in_1 \vec{g} + \vec{F}_{D,lg} \tag{16}$$

Gas phase (dispersed phase)

$$\frac{\partial}{\partial t}\left(\rho_g \cdot \in_g \cdot \vec{u_g}\right) + \nabla.\left(\rho_g \cdot \in_g \cdot \vec{u_g}\vec{u_g}\right) = \in_g.\nabla P + \nabla.\left(\in_g \mu_{\text{eff},g}\left(\nabla \vec{u_g} + \left(\nabla \vec{u_g}\right)^T\right)\right) + \rho_g.\in_g \cdot \vec{g} + \vec{F}_{D,lg} \tag{17}$$

where P is pressure, which is shared by both the phases and μ_{eff} is the effective viscosity. The term of the above momentum equations represents the interphase drag force between the two phases. Other interphase forces like the Bassett force, the virtual mass force, the lift force are neglected in the present study based on the recommendations of Khopkar et. al. (22). The drag force between the gas and liquid phases is represented by the equation

$$\vec{F}_{D,lg} = C_{D,lg}\frac{3}{4}\rho_1 \frac{\in_g}{d_b}|\vec{u_g} - \vec{u_1}|\left(\vec{u_g} - \vec{u_1}\right) \tag{18}$$

where the drag coefficient exerted by the dispersed gas phase on the liquid phase is obtained by the modified Brucato drag model (22), which accounts for interphase drag by microscale turbulence and is given by

$$\frac{C_{D,lg} - C_D}{C_D} = 6.5 \times 10^{-6}\left(\frac{d_b}{\lambda}\right)^3 \tag{19}$$

where λ is the Kolmogorov length scale, d_b is the bubble diameter, C_D is the drag coefficient of single bubble in a stagnant liquid and is given by

$$C_D = \text{Max}\left(\frac{24}{Re_b}(1 + 0.15Re_b), \frac{8}{3}\frac{Eo}{Eo + 4}\right) \tag{20}$$

where Eo is Eotvos number, Re_b is the bubble Reynolds number and they are given by

$$Re_b = \frac{|\vec{u_1} - \vec{u_g}|d_b}{\nu_1} \tag{21}$$

$$Eo = \frac{g(\rho_1 - \rho_g)d_b}{\sigma} \tag{22}$$

Turbulence models The turbulence model applied to the continuous liquid phase is the standard k–ε turbulence model. The corresponding values of k and ε are obtained by solving the following transport equations for the turbulence kinetic energy and turbulence dissipation rate:

$$\frac{\partial(\in_l \rho_l k)}{\partial t} + \nabla \cdot (\varepsilon_l \rho_l k u_l) - \nabla \cdot \left[\varepsilon_l\left(\mu + \frac{\mu_{tl}}{\sigma_k}\right)\nabla k\right] = \in_l (P_l - \rho_l \varepsilon) \tag{23}$$

$$\frac{\partial(\in_l \rho_l \varepsilon)}{\partial t} + \nabla \cdot (\varepsilon_l \rho_l \varepsilon u_l) - \nabla \cdot \left[\varepsilon_l\left(\mu + \frac{\mu_{tl}}{\sigma_k}\right)\nabla \varepsilon\right] = \in_l \frac{\varepsilon}{k}(C\varepsilon_1 P_l - C\varepsilon_2 \rho_l \varepsilon) \tag{24}$$

where μ_{tl} is the liquid phase turbulence viscosity or shear induced eddy viscosity, which is calculated based on the k–ε model as

$$\mu_{tl} = c_\mu \rho_l \frac{k^2}{\varepsilon} \tag{25}$$

where $C_{\varepsilon 1} = 1.44$, $C_{\varepsilon 2} = 1.92$, $\sigma_k = 1.0$, $\sigma_\varepsilon = 1.3$ and P_l is the turbulence production due to viscous force and is given by

$$P_1 = \mu_{tl}\nabla \vec{u_1} \cdot \left(\nabla \vec{u_1} + \nabla \vec{u_1}\right) - \frac{2}{3}\nabla \cdot \vec{u_1}\left(3\mu_{tl}\nabla \cdot \vec{u_1} + \rho_1 k_1\right) \tag{26}$$

For the continuous phase (liquid phase) the effective viscosity is calculated as

$$\mu_{\text{eff},l} = \mu_l + \mu_{tl} + \mu_{tg} \tag{27}$$

where μ_l is the liquid viscosity, and μ_{tg} represent the gas phase induced turbulence viscosity and is given by

$$\mu_{tg} = c_{\mu p}\rho_1 \in_g d_b |\vec{u_g} - \vec{u_1}| \tag{28}$$

where $C_{\mu p}$ has a value of 0.6.

For the dispersed gas phase the effective viscosity is calculated as

$$\mu_{\text{eff},l} = \mu_g + \mu_{T,g} \tag{29}$$

where $\mu_{T,g}$ is the turbulence viscosity of gas phases. No turbulence model is applied to the dispersed gas phase but the turbulent viscosity of the gas phase is related to the turbulence viscosity of the liquid phase by the following equation:

$$\mu_{T,g} = \frac{\rho_g}{\rho_l}\mu_{tl} \tag{30}$$

Bubble breakup model The net source to group i due to break up in Eq. (13) is

$$B_{B_i} = \rho_g \varepsilon_g \left(\sum_{j \text{N} i} B_{ji} f_i - f_i \sum_{j \text{b} i} B_{ij}\right) \tag{31}$$

where B_{ij} is the specific breakup rate (the rate at which bubbles from group i break into bubbles to form group j). The breakup rate is assumed to be a function of the breakup fraction as

$$B_{ij} = B'_{ij}\int_{f_{BV}} df_{BV} \tag{32}$$

where $m_i = \frac{\pi}{6}\rho_g d_i^3$ and f_{BV} is given by the equation

$$f_{BV} = \frac{m_j}{m_i} \tag{33}$$

The model used for bubble breakup kernel in present study is the model proposed by Luo and Svendsen (23). This model is based on the theory of isotropic turbulence and probability and according to this model, the breakup rate of bubbles of size i into bubbles of size j is modeled as

$$B'_{ij} = C_B(1 - \varepsilon_g)\left(\frac{\varepsilon}{d_i}\right)^{1/3}\int_{\xi_{min}}^{1}\frac{(1+\xi)^2}{\xi^{11/3}} \times \exp\left(-\frac{12\left(f_{BV} + (1 - f_{BV})^{2/3} - 1\right)r}{\beta\rho_l \varepsilon^{2/3} d_i^{5/3}\xi^{11/3}}\right)d\xi \tag{34}$$

where σ is the surface tension, and ξ is the dimensionless size of eddies in the inertial sub range of isotropic turbulence. The lower limit of the integration is given by

$$\xi_{min} = 11.4\frac{1}{d_i}\left(\frac{1}{\varepsilon}\nu_1\right)^{1/4} \tag{35}$$

where ε is the liquid phase eddy dissipation rate, and ν is the kinematic viscosity and the values of constants c_B, β are 0.923 and 2.

Bubble coalescence model The net source to group i due to coalescence in Eq. (13) is given by the following equation

$$B_{C_i} = (\rho_g \varepsilon_g)^2\left(\frac{1}{2}\sum_{j \le i}\sum_{k \le i} C_{jk} f_j f_k \frac{m_j + m_k}{m_j m_k} X_{jki} - \sum_k C_{ij} f_i f_j \frac{1}{m_j}\right) \tag{36}$$

where C_{ij} is the specific coalescence rate between groups i and j. X_{jki} is the fraction of mass due to coalescence between groups j and k, which goes into group i.

$$\begin{aligned} X_{jki} &= \frac{(m_j + m_k - m_{i-1})}{m_i - m_{i-1}} && \text{if } m_{i-1} < m_j + m_k < m_i \\ &= \frac{m_{i+1} - (m_j + m_k)}{m_{i+1} - m_i} && \text{if } m_i < m_j + m_k < m_{i+1} \\ &= 0 && \text{otherwise} \end{aligned} \tag{37}$$

The coalescence model from Prince and Blanch (24) is used in the present study. It describes the coalescence process as occurring in three steps: a first step where the bubbles collide and trap a layer of liquid between them, a second step where this liquid layer drains until it reaches a critical thickness, and a last step during which this liquid film disappears and the bubbles coalesce. The collisions between bubbles may be caused by turbulence, buoyancy or laminar shear. Only the first cause of collision (turbulence) is considered in the present model. Indeed collisions caused by buoyancy cannot be taken into account as all the bubbles from each class move at the same speed. The coalescence process is therefore modeled by a collision rate of two bubbles and a collision efficiency relating the time required for coalescence:

$$C_{ij} = F_C S_{ij} \left(u_{ti} + u_{tj}\right)^{1/2} \eta_{ij} \tag{38}$$

where F_C is a calibration coefficient. The collision efficiency is modeled by comparing the time required for coalescence t_{ij} with the actual contact time during the collision τ_{ij}.

The collision efficiency η_{lj} is modeled by comparing the time required for coalescence t_{ij} with the actual time during the collision s_{ij}

$$\eta_{ij} = e^{\left(-t_{ij}/\tau_{ij}\right)} \tag{39}$$

$$t_{ij} = \left(\frac{\rho_l r_{ij}^3}{16\sigma}\right)^{1/2} ln\left(\frac{h_0}{h_f}\right) \tag{40}$$

$$\tau_{ij} = \frac{r_{ij}}{\varepsilon^{1/3}} \tag{41}$$

where h_0 is the initial film thickness which is set equal to 1×10^{-4} m, h_f is the critical film thickness when rupture occurs, which is set equal to 1×10^{-8} m, and r_{ij} is the equivalent radius

$$r_{ij} = \left(\frac{1}{2}\left(\frac{1}{r_i} + \frac{1}{r_j}\right)\right)^{-1} \tag{42}$$

The cross-sectional area of the colliding particles is defined by

$$S_{ij} = \frac{\pi}{4}\left(d_i + d_j\right)^2 \tag{43}$$

The turbulent velocity is given by

$$u_{ti} = \sqrt{2}\left(\varepsilon d_i\right)^{1/3} \tag{44}$$

The calibration coefficient is set equal to 0.075.

Numerical methodology In this work, the commercial CFD software ANSYS CFX-11 is used for simulating the local hydrodynamic behavior gas–liquid stirred reactor with dual impellers. The details of the reactor geometry used for CFD simulation and the operating parameters are given in the experimental section. Only half of the reactor along the vertical axis is considered as the computational domain due to the geometrical symmetry and is discretized using block structured grids which allows finer grids in regions where higher spatial resolutions are required. Around 150,000 total computational nodes are created using the structured hexa mesh option of ICEM CFD in order to get the grid independent solution for the flow. Fig. 2 depicts a typical mesh of the computational geometry used for the numerical simulation in this work.

Various approaches have been proposed in the literature to capture the flow field due to impeller rotation of stirred reactors (25). For the present study, we have used the multiple frame of reference (MFR) approach, which is one of the widely used methods in the literature for simulating the flow field in stirred reactors. In this approach, the tank is divided into two regions i.e., a rotating frame which encompasses the impeller and the flow surrounding it and a stationary frame which includes the tank, baffles and the flow outside the impeller frame. The flow characteristics of the inner region are used to provide boundary conditions for the outer region. Solution of the outer region is used to provide boundary conditions for the inner region. The boundary between the inner and outer region have to be selected in such a way that, the predicted results are not sensitive to its actual location. The interaction of inner and outer regions is accounted by a suitable coupling at the interface between the two regions where the continuity of the absolute velocity is implemented. The boundary between inner and outer region for the present simulation is located at $r/R = 0.6$. No-slip boundary conditions are applied on the tank walls and shaft. The free surface of tank is considered as the degassing boundary condition.

The discrete algebraic governing equations are obtained by element based finite volume method. The second order equivalent to high-resolution discretization scheme is applied for obtaining algebraic equations for momentum, volume fraction of individual phases, turbulent kinetic energy and turbulence dissipation rate. Pressure velocity coupling was achieved by the Rhie Chow algorithm. The governing equations are solved using the advanced coupled multi grid solver technology of ANSYS CFX-11. The convergence criteria used in all the simulations is 1×10^{-4}, which is a factor by which the initial mass flow residual reduces as the simulation progresses. The simulations are carried out on the 8 noded, 32 processor AMD64 cluster with a clock speed of 2.55GH and 8 GB memory for each node.

RESULTS AND DISCUSSIONS

Bulk flow characteristics The gas–liquid flows generated by two six-bladed Ruston turbines in a stirred reactor are simulated for a single volumetric gas flow rate (Q_g) of 0.5 vvm and for three impeller

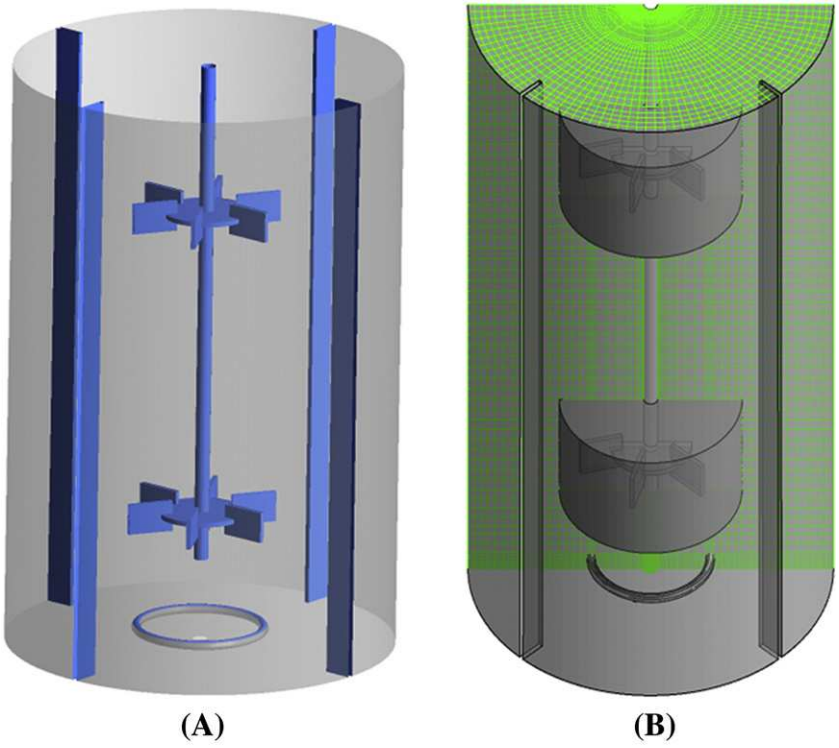

FIG. 2. (A) Reactor configuration (B) Computational grid used for simulation.

rotational speeds (N) equal to 250, 350, 450 rpm respectively. These values correspond to $Fl = 0.113$ and $Fr = 0.0343$, $Fl = 0.22$ and $Fr = 0.0245$ and $Fl = 0.367$ and $Fr = 0.0191$ respectively. Here Fl is the flow number, $Fl = Q_g/ND^3$ and Fr is the Froude number, $Fr = N^2D/g$, where Q_g is gas flow rate from sparger, N is impeller rotational speed and D is the impeller diameter. Under these experimental conditions, the fluid dynamics in the reactor represents FF, DL and DD flow regimes respectively, which is shown in Fig. 3. Here F stands for flooding regime, L stands for loading regime and D represents the fully dispersed regime.

It can be seen that for the impeller rotational speed of 250 rpm both lower and upper impellers are in flooding regime (FF). For impeller rotational speed of 350 rpm, the upper impeller shows fully dispersed regime while the lower impeller shows loading regime (DL). When the rotational speed of the impeller is 450 rpm, both upper and lower impellers show fully dispersed regime (DD). In DD regime, the gas bubbles get fully dispersed in the region underneath each of the impeller and/or radially outward. These type flow regimes are also reported by Shewale and Pandit, 2006 in their work.

Fig. 3 also shows the flow patterns obtained from CFD simulation for the same experimental parameter values. It can be seen clearly that excellent agreement exists between the experimental and CFD simulation results for the flow regimes in the aerated stirred tank with dual impellers. It can be seen from Fig. 3A that CFD simulation clearly shows the flooding regime of gas by both upper and lower impellers as observed in experiments when the impeller speed was 250 rpm. It can be clearly seen from the contour plot, that the gas from the sparger rises upwards without getting dispersed at both lower and upper impellers. Similarly from the contour plot in Fig. 3B, it can be seen that the gas bubbles are dispersed in the upper impeller but shows the loading regime in the lower impeller. Fig. 3C shows the fully dispersed regime of the gas bubbles in both the upper and lower impellers obtained by the CFD simulation. It can be quite clearly seen from the contour plot that the gas bubbles are dispersed underneath each of the impeller and/or radially outward.

The predicted liquid phase velocity vectors for all the three operating conditions are shown in Fig. 4A–C. It can be seen that the computational model is able to capture the different flow regimes for all the three operating conditions. For the case of FF regime ($Fl = 0.113$ and $Fr = 0.0343$), as shown in Fig. 4A there exists two separate circulation-loops for each impeller, one below the impeller and other one above the impeller. The bottom loop present in the reactor is formed due to the upward rising of gas bubbles from the sparger. The predicted liquid-phase velocity field for DL regime ($Fl = 0.22$ and $Fr = 0.0245$) is shown in Fig. 4B. Again it can be observed that there exists two-loop structure for DL flow regime also. However, the predicted two circulation-loop structure for DL flow regime is different from the two circulation-loop structure predicted for FF flow regime. The circulation loop at the bottom of the first impeller is small and this may be generated by the upward rising of the gas

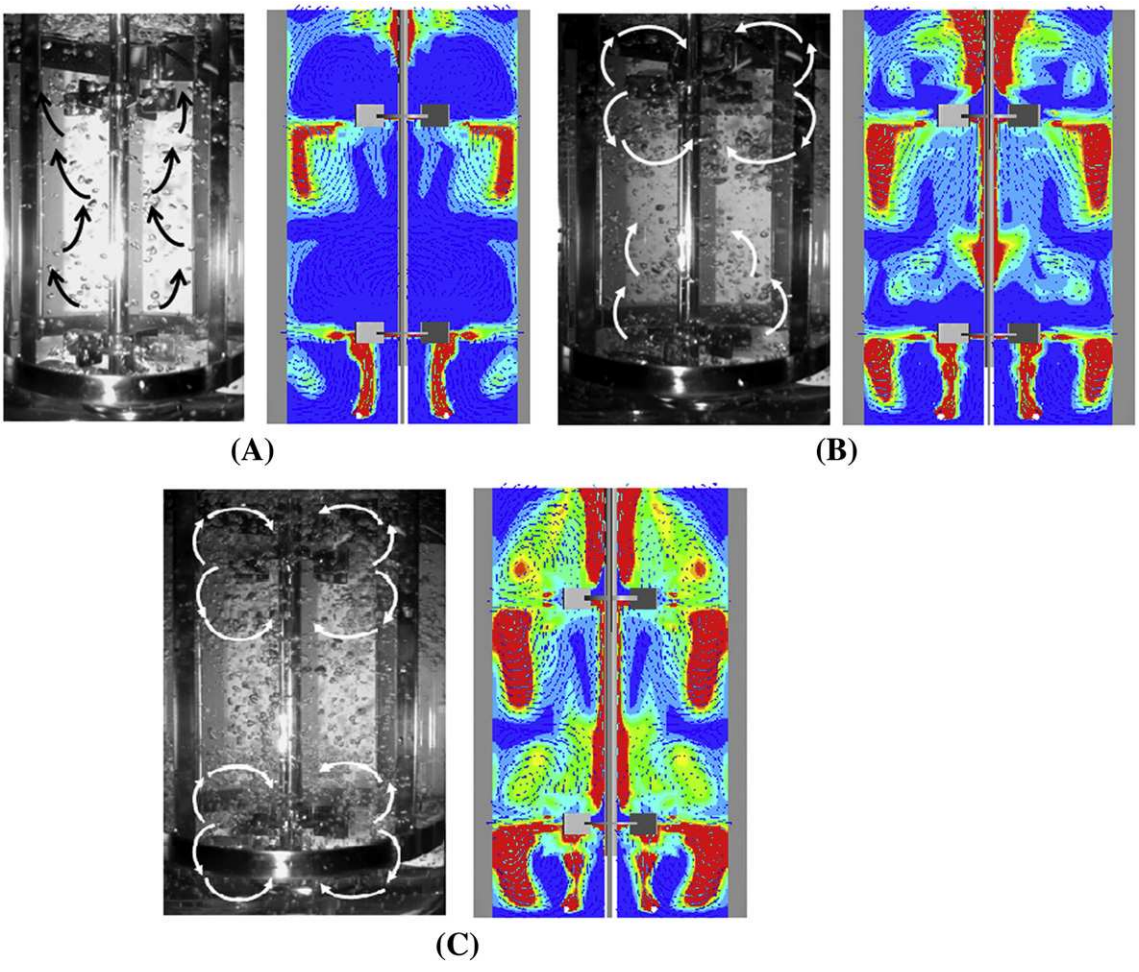

FIG. 3. Flow patterns observed from experiments along with the contour plots obtained from CFD simulation at the gas flow rate of 0.5 vvm (A) FF regime ($N = 250$ rpm) (B) DL regime ($N = 350$ rpm) (C) DD regime ($N = 450$ rpm).

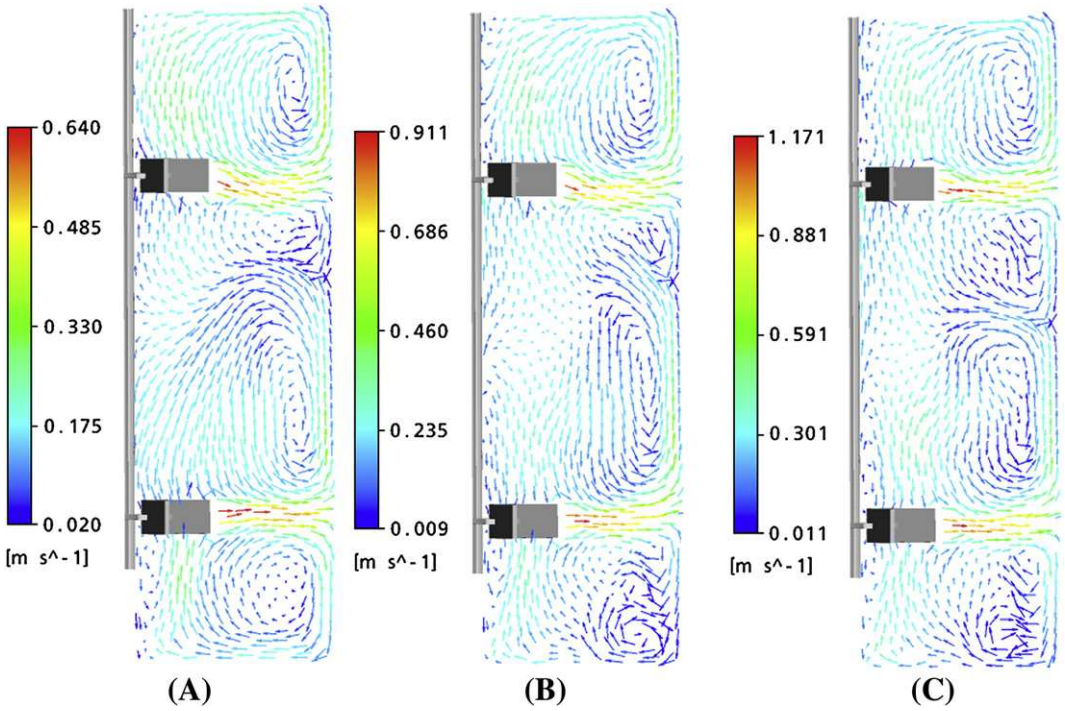

FIG. 4. Predicted liquid phase velocity profiles for different flow regimes at a gas flow rate of 0.5 vvm (A) FF regime ($N = 250$ rpm) (B) DL regime ($N = 350$ rpm) (C) DD regime ($N = 450$ rpm).

bubbles from the sparger in that region. The upper circulation-loop of bottom impeller interacts significantly with the bottom circulation-loop of upper impeller, unlike in the case of FF flow regime. Similarly, the predicted liquid-phase velocity field for DD regime ($Fl = 0.367$ and $Fr = 0.0191$) is shown in Fig. 4C. It can be seen from Fig. 4C that again there exists two circulation loops for each impeller and there is not much of an interaction between the upper loop of the lower impeller with the downward loop of the upper impeller. The lower circulation-loop of upper impeller is found to be significantly different from the other flow regimes (FF, and DL regimes) and also the length traveled by the liquid-phase through lower circulation-loop is more compared with the other two flow regimes. This may be due to fact that the pattern of flow in DD flow regime is more dominated by the impeller action than the dominance of upward rising gas in the region and hence, the liquid phase flow is just following the flow generated by impeller action.

Gas hold-up distribution The gas hold-up distribution in the reactor is strongly affected by the prevailing flow regimes and reactor internals. In the present study, the computational model is used to study the gas hold up distribution in FF, DL and DD flow regimes by varying the impeller rotational speed from 180 rpm to 540 rpm at two different gas flow rates of 0.3 vvm and 0.5 vvm. The gas hold up for various rotational speeds of the impellers obtained experimentally is shown in Fig. 5 for two different gas flow rates. It can be seen that the gas hold-up increases with an increase in stirring speed for different gas flow rates. This may be due to the fact that, at higher impeller speeds, very small bubbles are generated and they spend more time in the reactor. In addition at higher impeller speed the flow regime correspond to that of DD regime and hence favor higher gas hold up values.

Fig. 6 shows the gas hold up distribution obtained from CFD simulation for the air flow rate of 0.5 vvm and an impeller speed of

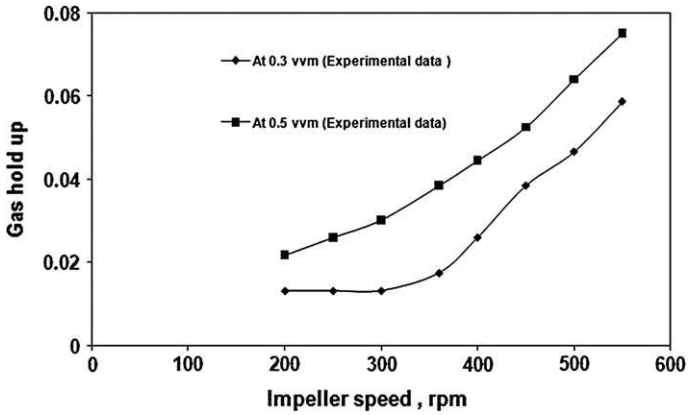

FIG. 5. Effect of impeller speed on gas hold-up values for different gas flow rates.

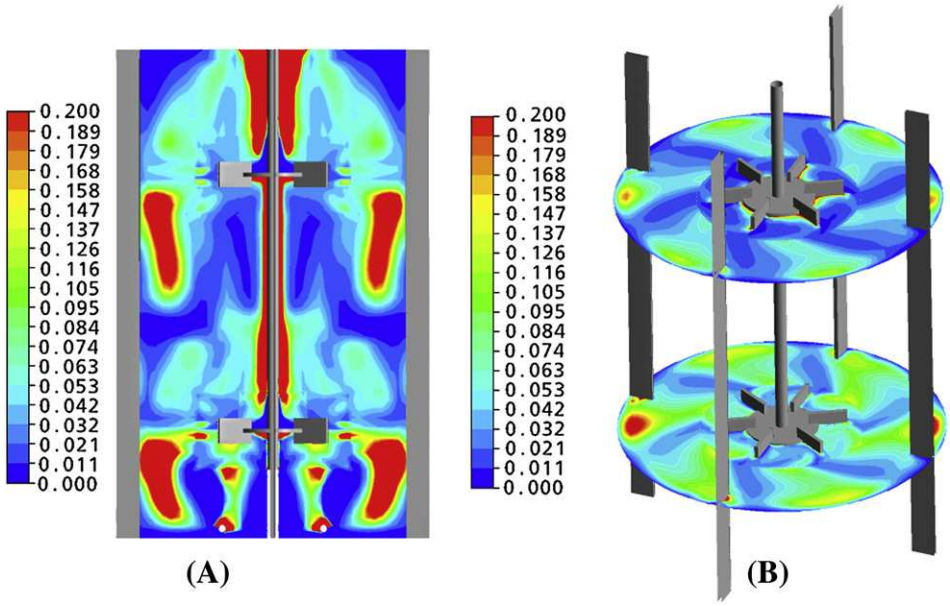

FIG. 6. Gas hold-up predicted by CFD simulation at the gas rate of 0.5 vvm at (A) midbaffle plane (B) two impeller planes.

450 rpm at mid-baffle plane. This flow regime corresponds to that of DD regime. It can be seen that the gas hold-up is more at the recirculating flow regions and at low-pressure region behind the impeller blades forming the so-called gas cavities. It can also be seen from Fig. 6A that the values of gas hold-up are higher in lower regions of tank and are lower in the upper regions of tank for both upper and lower impellers. This is due to fact that the flow generated by radial flow impeller leads to strong agitation at the bottom and at the tip of the impeller. Also the values of gas hold-up are more at the tip of the impeller due to breakage of bubbles by high shear produced by the impeller. The total gas hold-up predicted by CFD simulation is compared with the experimental data, and is shown in Table 1. It can be seen that the total gas hold-up predicted by present CFD simulation agrees well with the experimental data for the case of FF flow regime and over predicts for the case of DL and DD flow regime. One of the key reason of the observed over prediction of gas holdup may be due to the inaccurate estimation of inter-phase drag force as mentioned by Khopkar et al. (21).

Another gross characteristic which is of interest is power number and relative power input. The power number in stirred reactors are traditionally defined as

$$N_{p0} = \frac{P}{\rho N^3 D^5} \tag{45}$$

where N is the rotational speed in (rpm), D is the impeller diameter (m), and P is the actual power consumption. The relative power is the ratio of the aerated to unaerated power numbers, $\frac{N_{pg}}{N_{p0}}$. The Power draw (P) is determined from torque equation ($P=2\pi NT$) and total torque can be calculated from the torque acting on the all the blades. The predicted values of power number are compared with experimental data and they are listed in Table 1. From Table 1, it can be shown that the values predicted by CFD simulations agree reasonably well with the experimental values.

TABLE 1. Gross characteristics of gas–liquid stirred vessel for the air flow rate of 0.5 vvm.

Impeller speed (rpm)	Total gas hold-up		N_{Pg}/N_{P0}		Mixing time, s	
	Experiment	CFD	Experiment	CFD	Experiment	CFD
250	0.026	0.025	0.80	0.91	9.5	11.5
350	0.038	0.043	0.97	0.85	7.8	10.6
450	0.051	0.075	0.66	0.83	6.3	6.4

Mixing time Mixing time is one of the criteria which is used to characterize the liquid-phase mixing in stirred reactors. Mixing time is the time required to achieve a certain degree of homogeneity (26). The degree of homogeneity considered in the present study is 95% which means that the concentration variations are smaller than 5% of the fully mixed concentration. Fig. 7 shows the typical variation in the mixing time obtained from experimentally with impeller speed at a gas flow rate of 1.0 vvm. This variation of mixing time is found to depend on the flow regimes (flooding, loading, dispersion) in the gas–liquid agitated reactor. It can be seen from Fig. 7 that the mixing time decreases with increase in impeller speed in the initial stages of flooding regime. This is due to the fact that in this regime, the liquid mixing is mainly controlled by the liquid flow induced by the gas phase. When the impeller speed reaches the final stages of flooding regime, the liquid flow generated by the impeller causes local turbulence which in turn leads to more energy dissipation, and hence only less energy is available towards the liquid circulation and hence the mixing time increases. Further increase of impeller speed leads to DL flow regime in the gas–liquid agitated reactor. In this regime, the liquid circulation generated by the impeller is strong

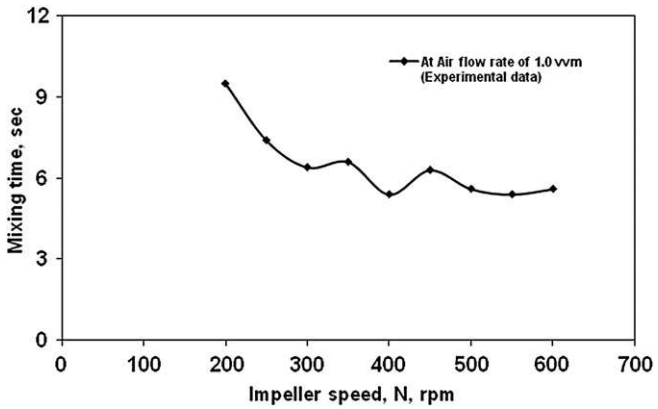

FIG. 7. Effect of impeller speed on mixing time for air flow rate of 1.0 vvm.

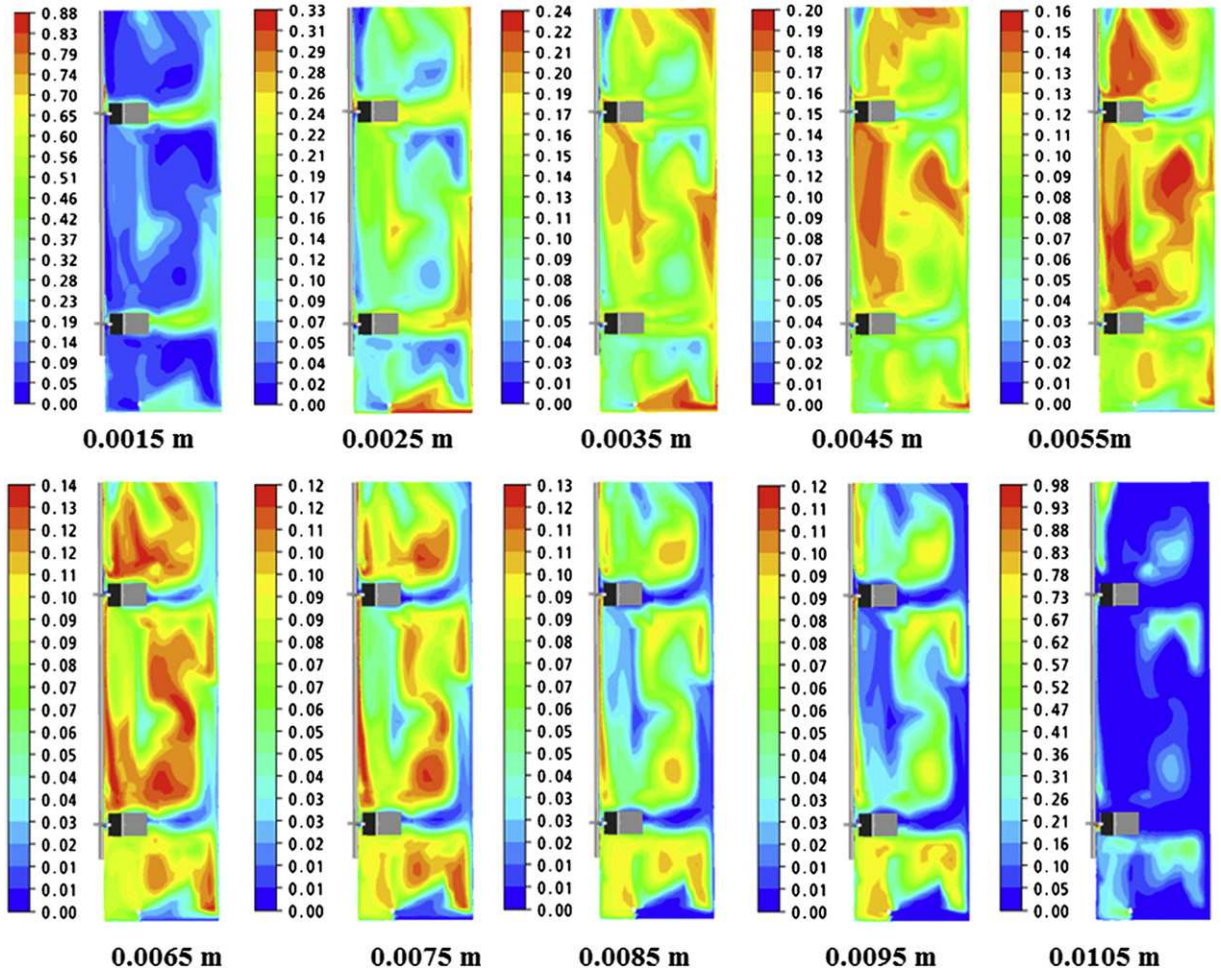

FIG. 8. CFD prediction of local bubble size distribution at an impeller speed of 450 rpm and for the air flow rate of 0.5 vvm.

enough to disperse the gas bubbles above the impeller leading to decrease in mixing time with further increase in impeller speed. If the impeller speed is further increased the flow regime changes from DL regime to DD regime. In this regime, each impeller creates a circulation cell around itself (Fig. 3) and mixing performance of the reactor is dominated by the exchange flow rate between the adjacent circulation cells instead of the overall circulation flow rate generated by each impeller and hence the mixing time increases sharply. A similar observation is also reported by Abrardi et al. (5) in their experimental investigation.

The mixing time obtained from CFD simulation is compared with experimental data and which is shown in Table 1. It can be seen that the CFD simulation over predicts the mixing time compared with the experimental observations. The turbulence model and inadequacies of inter-phase momentum exchange term are some of the possible reasons for the observed over-prediction. One of the key reasons of the observed over-prediction of mixing time might be due to inaccurate estimation of inter-phase drag force. Similarly, the prevailing levels of turbulence were estimated using the standard k–ε model of turbulence and the degree of turbulent intensity which mainly affects the prediction of mixing time in stirred tank reactor.

Model prediction of bubble size distribution In multiphase reaction processes, the dispersion and interfacial heat and mass transfer fluxes are closely related to the fluid dynamics of the system through gas–liquid contact area. Hence the dynamic changes of gas bubble diameters will play an important role in the study of multiphase reaction mechanisms. Hence we have used the CFD model for the prediction of transient dynamic behavior of bubble size distribution in the gas–liquid agitated reactor.

Fig. 8 is the CFD model predicted bubble size distribution of the gas liquid agitated reactor for the air flow rate of 0.5 vvm and the impeller speed of 450 rpm. Fig. 8 illustrates the CFD model predictions of the size fractions of the 10 bubble groups. Gas bubbles with diameters ranging from 1 to 1 to 11 mm are divided into 10 bubble groups, where the average diameter of each group is 1.5, 2.5, 3.5, 4.5, 5.5, 6.5, 7.5, 8.5, 9.5, 10.5 mm, respectively. It can be seen that small bubbles

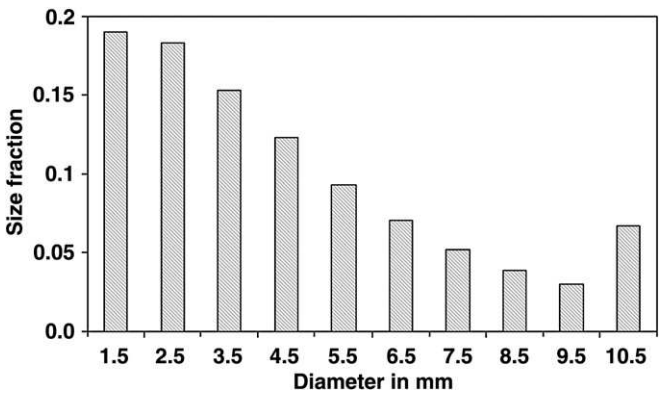

FIG. 9. Prediction of volume-averaged bubble size distribution of the stirred tank reactor at impeller speed of 450 rpm for air flow rate of 0.5 vvm.

viz. groups 1–5 (size range of 1.5–5.5 mm) are found in the impeller discharge region with size fractions mostly larger than 0.2. Since higher energy dissipation occurs at the impeller discharge region due to break up of large eddies into smaller eddies fine bubbles are formed at that region. The large bubbles viz. groups 6–10 (size range of 6.5 mm–10.5 mm) are found above and below the impeller regions with size fractions lesser than 0.2. The large size of bubbles at these regions may be due to the coalescence of bubbles. It should be noticed that there are locations with bubble class size fraction larger than 0.2 for group 10, which might be the result of sustaining bubble coalescence as there is obvious gas recirculation there. (refer to gas hold-up prediction in Fig. 5).

The volume averaged bubble size fractions of group 1–10 are calculated and shown in Fig. 9. It can be obviously seen from this plot that the small bubbles of groups 1–5 take a big part of all the gas bubbles; whereas large bubbles of groups 6–10 take only a small part of all the gas bubbles.

In the present work, we have carried out multiphase CFD simulation to identify various flow regimes and hydrodynamic parameters in gas–liquid stirred tank bioreactor with dual Rushton turbine impellers . The experimental part of the investigation has provided insight to the various flow regimes of the systems and hydrodynamic parameters obtained are used for validation of CFD simulation results. An Eulerian–Eulerian multiphase flow model along with population balance equation-multiple size group (MUSIG) model has been implemented. Breakup and coalescence of bubbles are modeled fundamentally using isotropic turbulence theory. The flow regimes of gas–liquid stirred tank bioreactor with dual-impeller predicted by CFD simulation is in excellent agreement with experimental observation. The hydrodynamics parameters of fractional gas hold-up, and mixing time were measured. It was found that gas hold-up increases with an increase in stirring speed for different superficial gas velocity and mixing time varies depending on the operating flow regimes prevailing in the system. Also the effect of gas flow rate and impeller speed on gas hold-up and power consumption have been investigated.

ACKNOWLEDGMENTS

R. Panneerselvam and Syed Ubaid Ahmed gratefully acknowledge the financial support for this work by Council of Scientific and Industrial Research (CSIR), Government of India.

References

1. **Gogate, P. R., Beenackers, A., and Pandit, A. B.:** Multiple impeller systems with a special emphasis on bioreactors: a critical review, Biochem. Eng. J., **6**, 109–144 (2000).
2. **Smith, J. M., Warmoeskerken, M., and Zeef, E.:** Flow conditions in vessels dispersing gases in liquids with multiple impellers, in: C. S. Ho, J. Y. Oldshue (Eds.), Biotechnology Processes, AIChE, 1987, pp. 107–115 (1987).
3. **Hudcova, V., Machon, V., and Nienow, A. W.:** Gas–liquid dispersion with dual Rushton turbine impellers, Biotech. Bioeng., **34**, 617–628 (1989).
4. **Abardi, V., Rovero, G., Sicardi, S., Baldi, G., and Conti, R.:** Sparged vessels agitated by multiple turbines, Proc. 6th Eur. Conf. Mixing, 329–336 (1988).
5. **Abrardi, V., Rovero, G., Sicardi, S., Baldi, G., and Conti, R.:** Hydrodynamics of gas–liquid dispersion with a multi impeller system, Chem. Eng. Res. Des., **68**, 516–522 (1990).
6. **Bouaifi, M., Roustan, M., and Djebbar, R.:** Hydrodynamics of multistage agitated gas–liquid reactors, Proc. 9th Eur. Conf. Mixing, 137–144 (1997).
7. **Vasconcelos, J. M. T. and Alves, S. S.:** Mixing in gas–liquid contactors agitated by multiple turbines in the flooding regime, Chem. Eng. Sci., **50**, 2355–2357 (1995).
8. **Vasconcelos, J. M. T., Alves, S. S., Nienow, A. W., and Bujalski, W.:** Scaleup of mixing in gassed multi-turbine agitated vessels, Can. J. Chem. Eng, **76**, 398–404 (1998).
9. **Vrabel, P., Van der lans, R., Cui, Y. Q., and Luyben, K.:** Compartmental model approach: mixing in large scale aerated reactors with multiple impellers, Chem. Eng. Res. Des, **77**, 291–302 (1999).
10. **Machon, V. and Jahoda, M.:** Liquid homogenization in aerated multi impeller stirred vessel, Chem. Eng. Tech., **23**, 869–876 (2000).
11. **Shewale, S. D. and Pandit, A. B.:** Studies in multiple impeller agitated gas–liquid contactors, Chem. Eng. Sci., **61**, 489–504 (2006).
12. **Gosman, A. D., Lekakou, C., Politis, S., Issa, R. I., and Looney, M. K.:** Multidimensional modeling of turbulent two-phase flows in stirred vessels, AIChE J., **38**, 1947–1956 (1992).
13. **Bakker, A. and van den Akker, H. E. A.:** A computational model for the gas–liquid flow in stirred reactors, Chem. Eng. Res. Des, **72**, 594–606 (1994).
14. **Ranade, V. V. and van den Akker, H. E. A.:** A computational snapshot of gas–liquid flow in baffled stirred reactors, Chem. Eng. Sci., **49**, 5175–5192 (1994).
15. **Ranade, V. V. and Deshpande, V. R.:** Gas–liquid flow in stirred reactors. Trailing vortices and gas accumulation behind impeller blades, Chem. Eng. Sci., **54**, 2305–2315 (1999).
16. **Wang, W. and Mao, Z.:** Numerical simulation of gas–liquid flow in a stirred tank with a Rushton impeller, Chin. J. Chem. Eng., **10**, 385–395 (2002).
17. **Lane, G. L., Schwarz, M. P., and Evans, G. M.:** Predicting gas–liquid flow in a mechanically stirred tanks, Appl. Math. Model., **26**, 223–235 (2002).
18. **Alves, S. S., Maia, C. I., Vasconcelos, J. M. T., and Serralheiro, A. J.:** Bubble size in aerated stirred tanks, Chem. Eng. J., **89**, 109–117 (2002).
19. **Alves, S. S., Maia, C. I., and Vasconcelos, M. T.:** Experimental and modeling study of gas dispersion in a double turbine stirred tank, Chem. Eng. Sci., **57**, 487–496 (2002).
20. **Kerdouss, F., Bannari, A., and Proulx, P.:** CFD modeling of gas dispersion and bubble size in a double turbine stirred tank, Chem. Eng. Sci., **61**, 3313–3322 (2006).
21. **Khopkar, A. R., Kasat, G. R., Pandit, A. B., and Ranade, V. V.:** CFD simulation of mixing in tall gas–liquid stirred vessel: role of local flow patterns, Chem. Eng. Sci., **61**, 2921–2929 (2006).
22. **Khopkar, A. R., Rammohan, A. R., Ranade, V. V., and Dudukovic, M. P.:** Gas–liquid flow generated by a Rushton turbine in stirred vessel: CARPT/CT measurements and CFD simulations, Chem. Eng. Sci., **60**, 2215–2229 (2005).
23. **Luo, S. M. and Svendsen, H.:** Theoretical model for drop and bubble breakup in turbulent dispersions, AIChE J., **42**, 1225–1233 (1996).
24. **Prince, M. and Blanch, H.:** Bubble coalescence and break-up in air sparged bubble columns, AIChE J., **36**, 1485–1499 (1990).
25. **Brucato, A., Ciofalo, M., Grisafi, F., and Micale, G.:** Numerical prediction of flow fields in baffled stirred vessels: a comparison of alternative modelling approaches, Chem. Eng. Sci., **53**, 3653–3684 (1998).
26. **Ranade, V. V., Bourne, J. R., and Joshi, J. B.:** Fluid mechanics and blending in agitated tanks, Chem. Eng. Sci., **46**, 1883–1893 (1991).